Theory of Stark spectroscopy transients from thin film organic semiconducting devices

Roderick C. I. MacKenzie*
Faculty of Engineering, University of Nottingham, Nottingham NG7 2RD, United Kingdom

Anna Göritz
Institute of Physics, Hermann-Herder-Straße 3a, D-79104 Freiburg, Germany

Steve Greedy
Faculty of Engineering, University of Nottingham, Nottingham NG7 2RD, United Kingdom

Elizabeth von Hauff
Physics of Energy, Department of Physics and Astronomy, Vrije Universiteit Amsterdam, De Boelelaan 1081, 1081 HV Amsterdam, The Netherlands

Jenny Nelson
Department of Physics, Imperial College London, South Kensington Campus, London SW7 2AZ, United Kingdom and FRIAS, University of Freiburg, Albertstraße 19, 79104 Freiburg, Germany

(Received 2 December 2013; revised manuscript received 18 March 2014; published 21 May 2014)

Herein, we propose a model to describe picosecond-nanosecond charge separation and nongeminate recombination in organic semiconductors. The model is used to explain time-resolved electroabsorption (EA) measurements performed on diodes made from phenyl-C61-butyric acid methyl ester. We find that the measured shape of the EA transient is due to a combination of microscopic carrier dynamic effects such as carrier trapping, as well as macroscopic effects such as band bending caused by the nonuniform poloron generation profile across the device. We demonstrate that the initial fast phase of the EA transient is due to hot free carriers being able to move freely within the device; over time these hot free carriers cool and become trapped giving rise to the second slower phase of the transient. We further show that the commonly observed dependence of the EA signal on probe wavelength can be explained in terms of the spatial overlap of electrostatic potential within the device and the optical mode of the probe light. Finally, we discuss the implications of these results for pump-probe experiments on thin organic films.

DOI: 10.1103/PhysRevB.89.195307 PACS number(s): 73.61.Wp, 78.66.Tr, 73.50.−h, 72.80.Rj

I. INTRODUCTION

Within the last 12 years the efficiency of organic photovoltaic (OPV) devices has rapidly increased from 2% in 2001 to above 10% today [1]. However, for OPV devices to find commercial applications, their efficiency must be further increased. Key to further boosting cell efficiency is developing a full understanding of the physical mechanisms governing cell operation. The five key physical mechanisms governing the operation and efficiency of OPV devices are (1) exciton generation [2], (2) exciton dissociation [3], (3) charge separation [4,5], (4) charge transport [6,7], and (5) nongeminate charge recombination [8–10]. Steady-state transport and nongeminate recombination have received considerable attention [9,11–14] and as a result understanding of these processes has considerably improved. Recently Shockley-Read-Hall (SRH) recombination has been identified as being able to describe nonequilibrium carrier trapping and nongeminate recombination in working organic solar cells [8]. However, the physical description of early time scale (picosecond) charge generation and geminate recombination has received less attention within device models. A typical approach is to invoke a competition between geminate pair recombination and field-dependent pair separation [15]. However such an approach is not closely supported by experimental measurements of charge separation.

Recently, the observation of a time-resolved Stark shift in the electroabsorption (EA) signal has been used to probe the dynamics of charge carriers within the first few picoseconds after laser excitation within polymer:fullerene blends [16,17] and fullerene [18] devices. In these experiments a short ($\approx$150 fs) laser pulse is used to photoexcite excitonic states across the sample and a high external field of around (1 MV m^{-1}) is applied to force dissociation. In studies of PCBM (phenyl-C61-butyric acid methyl ester) by Cabanillas-Gonzalez *et al.* the excitons are seen to dissociate instantaneously into electrons and holes then start drifting towards the contacts [18]. The dipole formed between the electrons and holes drifting towards opposite contacts partially shields the active region from the externally applied field. Due to the change in average internal field within the sample, the EA peak at 2.3 eV changes in magnitude [18,19]. This change in electroabsorption can be used to monitor the internal field within the sample and hence the spatial separation of the electrons and holes [20].

In this paper we use a time domain device model to describe the early-time Stark response of a PCBM diode [18]; we choose to model a PCBM diode rather than a polymer:fullerene blend in order to simplify interpretation of the results and

*roderick.mackenzie@nottingham.ac.uk

because reliable experimental data exist. The model describes nongeminate recombination and carrier trapping using a mechanism similar to one which has previously been used to describe the steady-state JV curve and slow (microsecond) transient measurements from disordered organic materials [8]. Thus we demonstrate a model which can describe both the fast carrier dynamics a few picoseconds after generation and the slower (ns-μs) recombination processes which define the JV curve and thus efficiency in organic devices. We then apply this model to understand the time-resolved Stark spectroscopy data presented by Cabanillas-Gonzalez *et al.* The result is a better understanding of EA data from films of organic molecules.

II. EXPERIMENTAL DATA

In pump-probe Stark spectroscopy measurements, the field-induced change in transmission is given as

$$\Delta^2 T/T = (\Delta T/T)_F - (\Delta T/T), \tag{1}$$

where $(\Delta T/T)_F$ is the transmitted probe signal under field and $(\Delta T/T)$ is the transmitted probe signal under no field. Figure 1 plots Stark spectroscopy data for a PCBM diode as a function of time at different fields obtained by Cabanillas-Gonzalez *et al.* The pump laser was applied at time 0 and had an energy of 3.2 eV, power density of 0.35 mJ cm^{-2}, and pulse length of 180 fs [18]. The solid lines within the picture represent the fit of the model (described in detail later) to the experimental data. The inset of Fig. 1 plots the maximum of the probe signal before the laser pulse is applied against the applied field. The magnitude of the electroabsorption signal is known to change as the square of the field [18],

$$F(t) = (EA/A)^{\frac{1}{2}}. \tag{2}$$

Using linear regression the constant A was found to be 2.5×10^{-13} au m^2/V^2 (see the inset of Fig. 1). Equation (2) can be used to transform the transient Stark data after the application of the laser pulse in Fig. 1 to a value of average internal field. Once the average internal field within the device

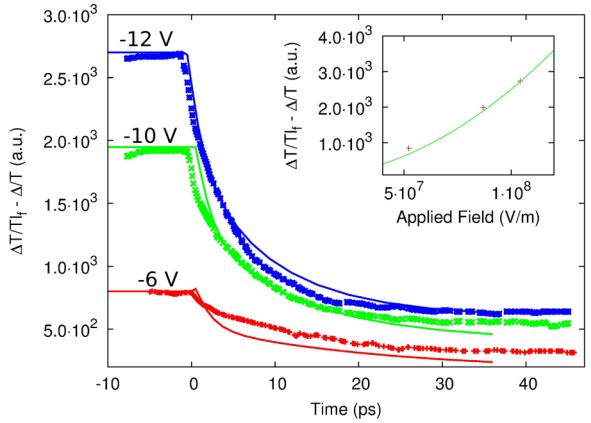

FIG. 1. (Color online) Evolution of the electroabsorption signal under different applied fields. Simulated (lines) and experimental (points; Cabanillas-Gonzalez's *et al.*). Inset: Electroabsorption signal vs field before application of the laser pulse ($t < 0$); the curve is used to transform measured electroabsorption signal to internal electric field.

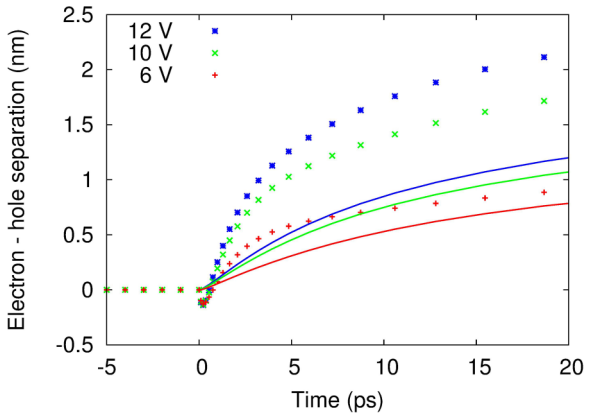

FIG. 2. (Color online) Charge separation distance extracted from EA data using Eq. (3) (points). Charge separation data taken directly from numerically calculated carrier profile of the model (lines). The difference between the two data sets is due to Eq. (3) only considering the microscopic separation of electron hole pairs.

is known, by treating the separating charge pairs as electric dipoles with in a unit volume, the following expression can be derived to relate change of internal field to electron-hole displacement,

$$r(t) = \frac{\epsilon_0 \epsilon_r [F_0 - F(t)]}{qn}, \tag{3}$$

where r is the charge pair separation distance, F_0 is the field before the laser pulse is applied, $F(t)$ is the field intensity at time t, n is the dipole density, ϵ_0 is the permittivity of free space, ϵ_r is the relative permittivity (see the Supplemental Material [43] for a full derivation), and q is the charge on an electron. The charge carrier separation distance extracted from the Stark data is shown in Fig. 2 as symbols.

Once the charge carrier pair separation distance and the field within the device are known, an instantaneous mobility can be defined using

$$\mu = \frac{dr(t)}{dt} \Big/ F(t). \tag{4}$$

This is plotted in Fig. 3 as the lines with points.

Equation (3) and therefore the above analysis assumes that the measured change in EA signal can be fully described by simply considering the microscopic process of bound pair disassociation. In this interpretation of the experimental results, the microscopic dipole generated by the separating electron and hole shields the medium between them from the externally applied field. This local reduction in field leads to a reduction in the EA signal. It is assumed that there is a uniform distribution of dipoles throughout the device with density n, that the change in field due to charge separation is also uniform across the device, and that changes to the electric field due to photoexcited carrier dynamics are only a perturbation to the applied field. These assumptions also implicitly assume that carrier generation, recombination, trapping, and transport are also uniform across the entire device. However, it is well known from previous studies that these processes vary strongly as a function of position. For example, the optical generation profile is known to have maxima and minima due

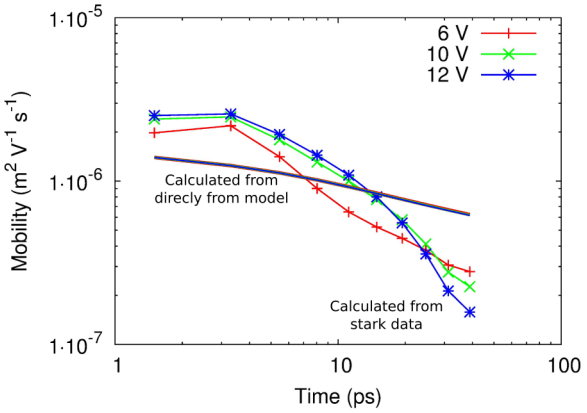

FIG. 3. (Color online) Instantaneous carrier mobility calculated from the EA data using Eq. (4) (lines + points), and the instantaneous carrier mobility numerically calculated from the model (lines).

to constructive and destructive interference of light within the device [21]. Furthermore, carrier injection and collection at the contacts will create carrier gradients within the device making charge fluxes vary as a function of position. The effect of nonuniform generation, injection from electrodes, and significant recombination are likely to influence the electric field profile and spatial distribution of excitons, thus influencing the EA response. In the following pages we develop a macroscopic numerical device model to describe carrier separation process across the whole device on the picosecond to nanosecond time scale. We then use this model to obtain a better interpretation of the experimental EA data.

III. NUMERICAL MODEL

The process of exciton generation, charge separation, carrier transport, trapping, and recombination must be described in the time domain along with the time-dependent and electrostatic effects. We use an effective medium approximation to model the fullerene layer [15,22]. To calculate the transient electric field within the diode, Poisson's equation is solved,

$$\frac{d}{dx}\epsilon_0\epsilon_r\frac{d\phi}{dx} = q(n_f + n_t - p_f - p_t), \tag{5}$$

between the anode ($x = 0$) and cathode ($x = d$), where ϵ_0 is the permittivity of free space, ϵ_r the relative permittivity of the medium, ϕ the (instantaneous) electrostatic potential, and q the electron charge. The transient densities of free electrons, trapped electrons, free holes, and trapped holes are given by n_f, n_t, p_f, p_t, respectively. To describe charge transport the drift diffusion equations are solved for positive and negative charge carriers

$$J_n = q\mu_e n_f\frac{\partial E_{\mathrm{LUMO}}}{\partial x} + qD_n\frac{\partial n_f}{\partial x}, \tag{6}$$

$$J_p = q\mu_h p_f\frac{\partial E_{\mathrm{HOMO}}}{\partial x} - qD_p\frac{\partial p_f}{\partial x}, \tag{7}$$

where J_n and J_p are the electron and hole carrier densities, D_n and D_p are the electron and hole diffusion coefficients, μ_e and μ_h are the carrier mobilities, and E_{LUMO} and E_{HOMO} represent the free carrier mobility edges. To force conservation of charges the carrier continuity equations are also solved.

In disordered materials such as those used in organic electronics, it is well known that the presence of localized trap states below the mobility edge [23–27] is a key factor in determining the transport properties [23]. The distribution of energies of such trap states influences the charge dynamics and the relationship between charge density and bias. It has recently been shown that in poly(3-hexylthiophene):phenyl-C61-butyric acid methyl ester (P3HT:PCBM) cells recombination can be described using the Shockley-Read-Hall (SRH) [8,22,28] mechanism in which carriers recombine when a free charge carrier of one polarity meets a trapped carrier of the other polarity. To account for carrier trap states within our model we introduce exponential distributions of trap states for both electrons,

$$\rho^e(E) = N^e\exp\left(E/E_u^e\right), \tag{8}$$

and holes,

$$\rho^h(E) = N^h\exp\left(E/E_u^h\right), \tag{9}$$

where ρ is the energy-resolved density of trap states, $N^{e/h}$ is the density of states at the mobility edge, and $E_u^{e/h}$ is the characteristic energy of the exponential tails. Although recent work suggests the trap distribution is more complex than a pure exponential [29], we use an exponential because it has been shown to reproduce experimental data well [22,28–30].

To calculate the spatial photon distribution within the device due to the 3.2 eV pump laser the transfer matrix method [31] is used. This calculates the forward and backward propagating electric fields within the multilayer device while taking into account interfaces between layers and absorption of the materials. The complex refractive index values for ITO, PEDOT, PCBM, and Au are taken from previously published data [32,33].

The full blue line in Fig. 4 plots the calculated modal profile of the pump light. It is assumed that every absorbed photon generates an electron-hole pair at time $t = 0$. The generation of charge within the model will change the local potential through Poisson's equation [Eq. (5)]. By solving Poisson's equation,

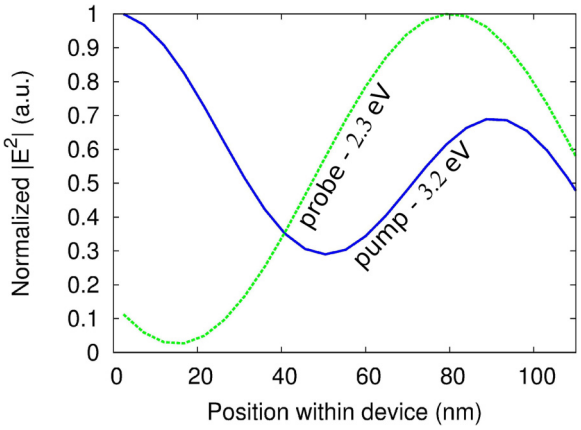

FIG. 4. (Color online) Calculated photon distributions of light within the solar cell for the pump and probe wavelengths of 3.2 eV and 2.3 eV, respectively.

Coulomb interactions between charges are always included in the model, so that the electric field charges experience is influenced by the presence of other charges within the device. Within this picture where all photogenerated charges are included, more and less mobile charges can be distinguished by the gradual relaxation of some of the charges into deeper lying trap states with a consequent reduction in their ability to take part in transport. Those charges that quickly relax into traps could be considered as equivalent to the charge pairs that do not succeed in dissociating within simpler models such as that used by Cabanillas-Gonzalez *et al.* The local contribution to the EA signal due to the sum of the internal and external fields can be calculated as

$$I(\omega,t,x) = C\left(\frac{d\phi}{dx}\right)^2, \tag{10}$$

where C is a constant. Therefore, the EA averaged over the entire device is given by

$$\Delta T/T(t,\omega) = d^{-1}\int_0^d I(\omega,t,x)m(x,\omega)dx, \tag{11}$$

where $m(x,\omega)$ is the normalized optical modal profile of the *probe* light. As with the pump light, the modal profile of the 2.3 eV probe light within the device over the ITO, PEDOT, PCBM, and the gold contact layer is calculated using a transfer matrix based approach. Thus, in a region of the device where there is constructive interference of the probe light $\Delta T/T(t,\omega)$ is very sensitive to changes in field at that location; however where there is destructive interference of the probe light the measurement is less sensitive to changes in local field at that location. The dashed green line in Fig. 4 plots the calculated modal profile of the 2.3 eV probe light.

The model was fitted to the data in Fig. 1; the result of the fit is shown as solid lines plotted with the experimental data (dots). The resulting model parameters are given in the Supplemental Material [43]. Figure 1 shows that with the given pump and probe wavelengths, the modeled EA signal shows a sharp drop upon excitation then decays more slowly. In the next section we examine carrier distributions within the device as a function of time and visualize the charge separation process.

IV. INTERPRETING ELECTROABSORPTION DATA FROM A PCBM DIODE

Figure 5(a) plots the distribution of carriers within the device just after photoexcitation at 3.2 eV. It can be seen that the initial carrier distribution follows that of the pump photon distribution plotted in Fig. 4 (blue line). A large negative potential (−6 V) has been applied to the right-hand side of the device; therefore as time increases the hole population will drift to the right and the electron population will slide to the left. As these sinusoidal charge carrier distributions pass over one another, dipoles will form where there is a net positive or negative charge. Such a dipole can be seen in Fig. 5(b) at 60 nm, where the net carrier density (hole minus electron) has been plotted at different times. At the right-hand side of Fig. 5(b) a sharp rise in hole density can be seen. This is due to the photogenerated electron sheet drifting to the left, exposing a net positive charge near the contact. A corresponding but smaller increase in the electron density can be seen on the left-hand side of the device. These local changes in charge density result in local potential changes and thus band bending. This can be seen in Fig. 5(c) where the LUMO level (electron mobility edge) has been plotted across the device as a function of time. From Figs. 5(a)–5(c), we can see that the local potential does not reduce uniformly throughout the device as a described by the simple analytical analysis in Sec. II. Instead, the local changes in potential are closely linked to how the initial macroscopic sinusoidal distribution of the photogenerated charge clouds drift/diffuse over each other.

Sometimes the pump wavelength is varied in an EA experiment [3,34,35] resulting in different shaped EA transients. In the next paragraphs we use the model to theoretically investigate how the chosen pump and probe wavelengths can affect the EA signal. Figure 6(a) plots the distribution of photogenerated charge carriers within the device when a pump energy of 2.5 eV is used instead of 3.2 eV. An excitation energy where absorption is weak may be chosen with the aim of generating charges uniformly across a device. The photogenerated carrier distribution at 2.5 eV [Fig. 6(a)] is significantly different from that at 3.2 eV [Fig. 5(a)]. A clear exponential decay can be observed in the distribution at 3.2 eV due to the high absorption of PCBM above 3.1 eV, whereas at 2.5 eV there is no exponential decay in the photon distribution

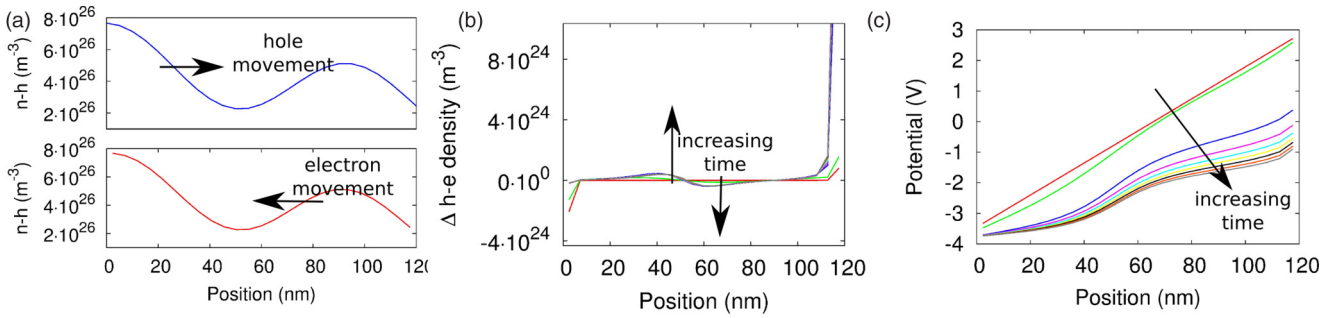

FIG. 5. (Color online) (a) Generation profile of charge carriers within device for a pump energy of 3.2 eV (blue line = hole density, red line = electron density), (b) corresponding difference between hole and hole electron populations as a function of time (holes minus electrons), and (c) resulting bending of the LUMO level within the device.

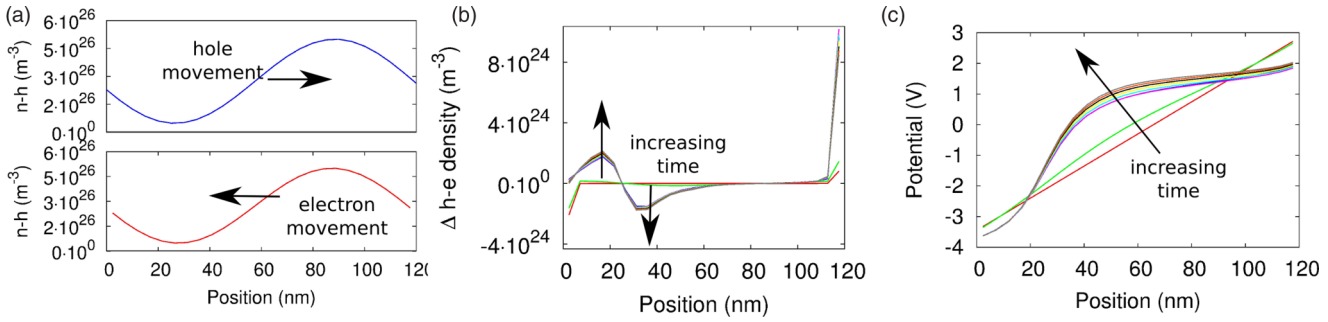

FIG. 6. (Color online) (a) Generation profile of charge carriers within the device for a pump energy of 2.5 eV (blue line = hole density, red line = electron density), (b) corresponding difference between hole and hole electron populations as a function of time (hole minus electrons), and (c) resulting bending of the LUMO level within device. Note, by changing the pump wavelength from 3.2 eV (Fig. 5) to 2.5 eV, the LUMO band bending is significantly altered. This will also affect the corresponding EA signal.

due to the low absorption of PCBM at this energy. The spatial period of the light can also be seen to be longer at 2.5 eV than at 3.2 eV.

Figure 6(b) plots the corresponding net carrier (hole minus electron) density within the device. By comparing Fig. 6(b) and Fig. 5(b), it can be seen that changing the pump energy has shifted the photoinduced charge dipole from 60 nm to 25 nm and increased its magnitude. The influence this photogenerated charge distribution has on the potential within the device can be seen in Fig. 6(c), where the LUMO has again been plotted as a function of time. The LUMO can be seen to bow upwards due to the macroscopic charge dipole centered around 25 nm. The band bending resulting from pumping at 2.5 eV is very different from that observed when the device is pumped at 3.2 eV. Since the EA signal is proportional to the average of the square of the electrostatic field within the device (i.e., how much the bands are bent), we would therefore expect the EA signal from a device pumped at 3.2 eV to be very different from a device pumped at 2.5 eV.

The blue line in Fig. 7 plots the EA signal corresponding to Figs. 6(a)–6(c). It can be seen that after photoexcitation (at time = 0), there is a sudden reduction in EA signal to a minimum at 5 ps, followed by a gradual increase in EA signal between 5 and 40 ps. In contrast, the corresponding EA response at a pump energy of 3.2 eV in Fig. 1 (−6 V; red line) shows a gradual reduction in EA signal between 0 and 40 ps. Thus from the above discussion we can say that the choice of pump energy will determine the initial spatial distribution of photogenerated carriers, which in turn determine where net positive or negative regions of charge within the device are generated and how the bands bend and thus the exact nature of the EA response.

Figure 7 also plots the simulated EA responses of the device when probed at 2.6 eV and 3.0 eV (still pumped at 2.5 eV). It can be seen from this figure that not only is the EA signal dependent on the pump energy, but also on the chosen probe wavelength. In fact a probe energy of 3.0 eV produces a positive EA response whereas a probe energy of 2.3 eV produces a negative response. This is because the measured EA signal is calculated by multiplying the square of the local electric field by the local photon density of the probe light [Eq. (11)]. Thus at a spatial position within the device where the probe light is at a maximum, the EA signal will be very sensitive to electrostatic potential changes; where the probe light is at a minimum, the EA signal will be less sensitive to potential changes. Thus different energies of probe light will sample the nonuniform potential gradients in Fig. 6(c) at different places. Figure 8 plots the spatial photon distributions of the 2.3 eV, 2.6 eV, and 3.0 eV probe light. It can be seen that the higher the probe energy the more photons there are between 0–50 nm and thus the more sensitive the EA signal will be to the band bending in Fig. 6(c) between 0 and 50 nm.

The impact of different light absorption profiles for pump and probe wavelengths is also relevant to time-resolved transient absorption measurements which are used to observe the evolution of excited states—particularly charge pair generation—on early (fs-μs) time scales following photoexcitation [35–39]. Although such experiments are often done on films, where optical interference effects are less pronounced than in devices with reflective back contacts, the effects of different pump and probe wavelengths on the spatial generation of charges and internal electrostatic fields are still significant. For example, in a recent study of ultrafast transient absorption in blend films of poly[2,1,3-benzothiadiazole-4,7-diyl[4,4-bis(2-ethylhexyl)-4H-cyclopenta[2,1-b:3,4-b] dithiophene-2,6-diyl]:Phenyl-C61-butyric acid methyl ester

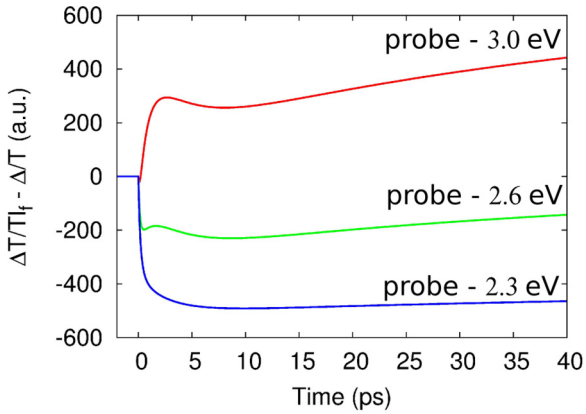

FIG. 7. (Color online) EA signals for a device pumped at 2.4 eV and probed at 2.3 eV, 2.6 eV, and 3.0 eV. It can be seen that by changing the probe energy the EA signal can be significantly altered. This is because different probe energies will have different photon distributions (see Fig. 8) within the active layer of the device, and thus probe the nonlinear band bending of the device at different spatial locations.

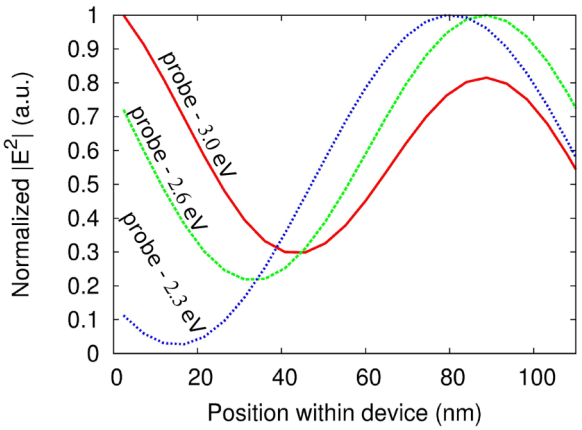

FIG. 8. (Color online) Normalized modal profiles of the probe light for photon energies of 2.3 (blue), 2.6 (green), and 3.0 eV (red). It can be seen that as photon energy is increased the photon density on the left-hand side of the device increases. Thus at low photon energies the EA measurement will only be sensitive to band bending on the right-hand side of the device, while at higher photon energies, the EA measurement will be able to measure average band bending over the whole device.

(PCPDTBT:PC61BM) [3] the authors interpret transient absorption phenomena to the kinetics of exciton dissociation, charge carrier generation, and relaxation and stimulated emission, without considering any spatial variation in charge and exciton densities. They attribute changes in dynamics resulting from changes in pump photon energy solely to microscopic phenomena. However, the method we present above would predict a significant influence on the transient absorption as a result of the different pump (1.7–2.4 eV) and probe (0.8–1.5 eV) energies on the macroscopic response of charges in those experiments. Based on the above analysis, we would expect both microscopic carrier relaxation effects and the macroscopic effects to have influenced the recorded transient absorption signal in their measurements.

V. DISCUSSION

Above, we demonstrated that due to constructive and destructive interference the pump light will generate a spatial variation in the internal field electromagnetic of the device. These macroscopic effects were not taken into account in the derivation of the transient charge separation distance [Eq. (3)]. Thus, next we examine the validity of Eq. (3), by comparing the predicted carrier separation distance $r(t)$ to that calculated directly from the carrier populations within the model. Figure 2 plots the charge separation distance calculated directly from Stark data using Eq. (3). Also plotted in the same figure is the carrier separation distance calculated directly from the modeled internal charge distributions within the model using a geometric average (lines),

$$\langle x_n \rangle = \frac{\int_0^d [n_f(x) + n_t(x) - n_i] x dx}{\int_0^d n_f(x) + n_t(x) dx}, \qquad (12)$$

where n_i is the sum of the initial distributions of trapped and free electrons at the given applied bias, at a time just after the pump laser has generated carriers within the device. An analogous expression can be written for holes. To calculate the average electron-hole separation distance the geometric centers of the charge packets are subtracted $\langle x \rangle = \langle x_n \rangle - \langle x_p \rangle$. If Fig. 2 is examined, it can be seen that the charge separation distance calculated from the Stark data and the separation of electron and hole centers of mass obtained directly from the model 2 are significantly different. The ultrafast phase seen in the experimental data between 0–2 ps is far more gradual in the model and the dependence of separation on field is stronger in the experimental data. Furthermore, key to accurately evaluating the charge separation distance is correctly calculating the the density of photogenerated charge pairs n [Eq. (3)]. For the experimental data in Fig. 2, Cabanillas-Gonzalez *et al.* estimated the value of 4.6×10^{24} m^{-3} by estimating the absorption cross section of the $S_1 - S_n$ states, while using a transfer matrix model to directly calculate the exciton density yields a value of 2.88×10^{26} m^{-3}. When calculating the curves in Fig. 2, we used the value of 4.6×10^{24} m^{-3} for consistency with Cabanillas-Gonzalez *et al.* However, we stress that the total photogenerated exciton density also influences the charge dynamics and separation velocity in our model, mainly as a result of the nonuniform electric field in the device.

If Fig. 2 is examined it can be seen that at early times (<10 ps) the average charge separation distance increases rapidly; however after this point the charge separation process slows. We can explain this trend by examining what happens to the photoinduced charge within our model as a function of time. Figure 9 plots the time evolution of the density of both free and trapped charge carriers under an applied field of −6 V. It can be seen that immediately after photoexcitation,

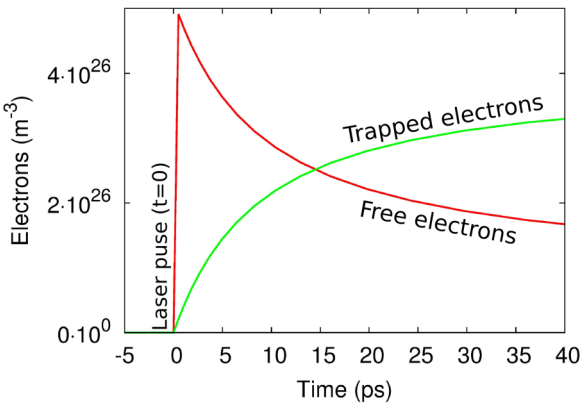

FIG. 9. (Color online) The average carrier density corresponding to free (hot) and trapped (cool) electrons during the measurement. Initially all photogenerated carriers are free but as they cool they become trapped. It can be seen that during the first 10 ps there are more free carriers than trapped carriers; this is the reason for the initial fast separation of the charge packets. It can be seen that past 10 ps most carriers are trapped and thus do not move; this is the reason for the second slow phase to the charge separation transient. At long times the number of trapped carriers decreases; this is due to recombination.

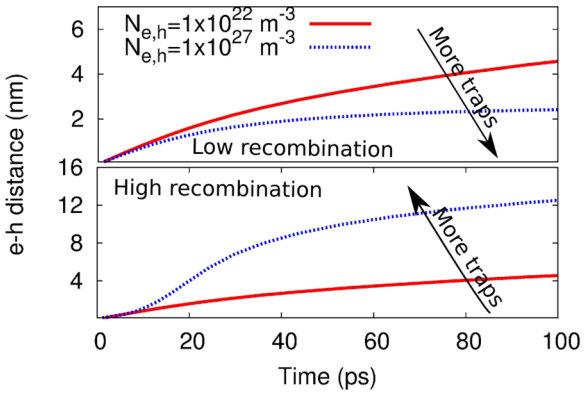

FIG. 10. (Color online) Influence of trap states on carrier separation distance. When recombination is low the traps act to arrest the separating charge populations. When recombination is high, recombination eats away at the charge packets and causes drift currents and increasing measured separation distance.

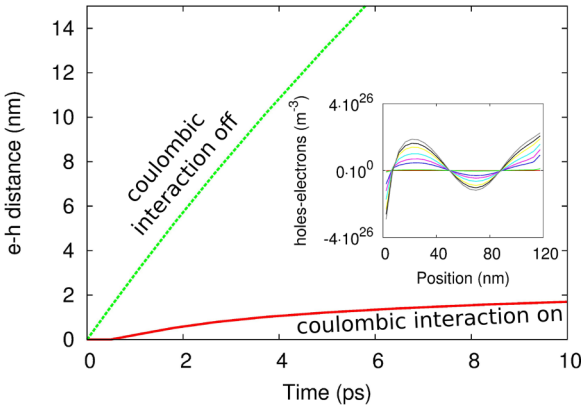

FIG. 11. (Color online) Simulated charge separation distance with the Coulombic effect of charge carriers taken into account (red line), and not taken into account within the simulations (green line). It can be seen that Coulombic attraction significantly slows the charge separation process. Inset: The photogenerated electron distribution subtracted from the hole population when Coulombic attraction is turned off. It can be seen that the peaks and troughs of the dipoles are much higher than in Figs. 5(b) and 6(b) due to the faster movement of charges.

free (hot) charge carriers dominate the carrier population; then as time passes and the carrier population cools the number of free charge carriers decreases as the number of trapped carrier increases. Thus there are two distinct regions of the measurement, the first when there are more free carriers than trapped carriers and the other when there are more trapped carriers than free carriers. When carriers are hot and free they can move; however once they become trapped movement becomes slow because they must detrap first.

Figure 10 (top) plots the calculated charge separation distance extracted directly from the model [using Eq. (4)] as a function of trap density. From the discussion in the previous paragraph, it would be expected that the higher the number of trap states in the material the faster hot carriers would relax into these states and so the slower charge separation would be. This can be seen in Fig. 10 (top) where a larger number of traps slow charge separation. However, when the recombination cross sections are increased [see Fig. 10 (bottom)], the influence of an increased density of trapped states is reversed. This is because more trap states will increase the rate of free-to-trapped carrier recombination; thus increased recombination will change the shape of the carrier clouds over time and so the macroscopic field within the device will also be altered. Therefore, when interpreting EA measurements, it is key to remember that what is being measured is the macroscopic field due to two macroscopic charge clouds moving away from one another rather than a microscopic process; therefore if the shape of the charge clouds changes due to recombination or other dynamic events then the estimated microscopic carrier separation distance will also change. We note that recombination is not usually invoked to describe fast dynamic effects but intensity-dependent recombination has previously been reported on the nanosecond and subnanosecond scale [40–42].

Figure 11 plots the average charge separation distance curve at −6 V (red line) from Fig. 2. Also plotted in Fig. 11 is the average charge separation distance curve for the same simulation where the Coulombic electron-hole interaction is turned off by setting the relative permittivity to 1×10^6 (green line); the inset to Fig. 11 plots the corresponding net charge profile (holes minus electrons) as a function of time. The simulations were carried out with a pump/probe wavelengths identical to those in Figs. 6(a)–6(c). It can be seen that the average charge separation distance increases much more rapidly when the Coulombic electron-hole interaction is turned off. If the inset is compared to Fig. 2(b), it can be seen that when there is no electron-hole attraction the net charge profile grows much more quickly as a function of time, also indicating the electron-hole populations are sliding over each other more quickly. All this suggests that the Coulombic electron-hole attraction is key to determining how fast the electrons and holes can move apart before becoming trapped and immobile. Indeed if Fig. 6(c) is examined there is a flattening of the LUMO centered around 60 nm which corresponds to the formation of a macroscopic charge dipole around 60 nm in Fig. 6(b). This flattening of the bands around the dipole is what is responsible for the slow charge separation in Fig. 11 when Coulombic interaction is turned on.

Cabanillas-Gonzalez *et al.* also defined a simple equation for calculating instantaneous carrier mobility [Eq. (4)]. However, mobility in disordered materials is known to be a strong function of carrier density; this is because the higher the carrier density, the more filled the deep trap states there will be and the are less likely it will be for photogenerated carriers to become trapped. As can be seen from Fig. 6(a), the charge density in the device varies as a strong function of position; thus it is difficult to define a single value of mobility for the device, so far away from equilibrium. One definition of mobility that has previously been used to define nonequilibrium mobility is

$$\mu_e = \frac{1}{d}\int_0^d \mu_{0e}\frac{n_{\text{free}}(x,t)}{n_{\text{free}}(x,t)+n_{\text{trap}}(x,t)}dx, \qquad (13)$$

where n_{free} is the density of free electrons, n_{trap} the density of trapped carriers, μ_0 the free carrier mobility, and x the position

within the device and d the thickness. An analogous expression can be defined for the holes.

Both Eq. (4) and Eq. (13) have been applied to extract the average carrier mobilities and the results are shown in Fig. 2. Here, we merely point that out that it is difficult to define a single value of mobility in nonequilibrium situations.

VI. CONCLUSION

We demonstrate that a model including trap states and Shockley-Read-Hall recombination can reproduce experimental charge separation data obtained with subpicosecond photoinduced Stark spectroscopy under a range of applied fields. We have demonstrated that at least part of the observed time-resolved electroabsorption signals is due to dynamic macroscopic charge carrier effects. A nonuniform charge carrier generation profile across the device leads to a nonuniform electrostatic potential profile. Probing at different wavelengths means that potential gradients at different spatial regions are preferentially probed. This varying spatial overlap between the nonuniform internal field and the modal profile of the probe light can significantly influence the measured EA signal. We demonstrate that macroscopic effects such as nongeminate recombination and band bending can significantly change the effective measured charge separation distance by changing the shape of the charge clouds. The model is able to explain why the measured charge separation distance initially increases rapidly then slows. In our model, the initial fast phase of the transient is due to unrelaxed or hot charge carriers moving freely within the device. Over time these hot carriers cool and become trapped giving rise to the second phase of the transient. We also discuss the implications of these results for other pump probe experiments. We recommend that different film thicknesses be used to check whether optical interference effects are indeed influencing the measured signal. With the aid of simple optical modeling this strategy could help transient electroabsorption measurements to result in a more complete picture of the charge carrier dynamics within the device.

[1] M. A. Green, K. Emery, Y. Hishikawa, W. Warta, and E. D. Dunlop, Prog. Photovolt: Res. Appl. **20**, 12 (2012).

[2] C. H. Woo, P. M. Beaujuge, T. W. Holcombe, O. P. Lee, and J. M. J. Frchet, J. Am. Chem. Soc. **132**, 15547 (2010).

[3] G. Grancini, M. Maiuri, D. Fazzi, A. Petrozza, H. Egelhaaf, D. Brida, G. Cerullo, and G. Lanzani, Nat. Mater. **12**, 29 (2013).

[4] T. M. Clarke and J. R. Durrant, Chem. Rev. **110**, 6736 (2010).

[5] D. Vithanage, A. Deviis, V. Abramaviius, Y. Infahsaeng, D. Abramaviius, R. MacKenzie, P. Keivanidis, A. Yartsev, D. Hertel, J. Nelson, V. Sundström, and V. Gulbinas, Nat. Commun. **4**, 2334 (2013).

[6] R. C. I. MacKenzie, J. M. Frost, and J. Nelson, J. Chem. Phys. **132**, 064904 (2010).

[7] M. M. Mandoc, F. B. Kooistra, J. C. Hummelen, B. de Boer, and P. W. M. Blom, Appl. Phys. Lett. **91**, 263505 (2007).

[8] R. C. I. MacKenzie, C. G. Shuttle, M. L. Chabinyc, and J. Nelson, Adv. Energy Mater. **2**, 662 (2012).

[9] M. Hilczer and M. Tachiya, J. Phys. Chem. C **114**, 6808 (2010).

[10] C. L. Braun, J. Chem. Phys. **80**, 4157 (1984).

[11] C. Groves and N. C. Greenham, Phys. Rev. B **78**, 155205 (2008).

[12] B. J. Tremolet de Villers, R. C. I. MacKenzie, J. J. Jasieniak, N. D. Treat, and M. L. Chabinyc, Adv. Energy Mater. **4**, 1301290 (2014).

[13] L. J. A. Koster, V. D. Mihailetchi, and P. W. M. Blom, Appl. Phys. Lett. **88**, 052104 (2006).

[14] R. A. Street, Phys. Rev. B **84**, 075208 (2011).

[15] L. J. A. Koster, E. C. P. Smits, V. D. Mihailetchi, and P. W. M. Blom, Phys. Rev. B **72**, 085205 (2005).

[16] D. A. Vithanage, A. Devižis, V. Abramavičius, Y. Infahsaeng, D. Abramavičius, R. C. I. MacKenzie, P. E. Keivanidis, A. Yartsev, D. Hertel, J. Nelson, V. Sundström, and V. Gulbinas, Nat. Commun. **4**, 2334 (2013).

[17] S. Gélinas, A. Rao, A. Kumar, S. L. Smith, A. W. Chin, J. Clark, T. S. van der Poll, G. C. Bazan, and R. H. Friend, Science **343**, 512 (2014).

[18] J. Cabanillas-Gonzalez, T. Virgili, A. Gambetta, G. Lanzani, T. D. Anthopoulos, and D. M. de Leeuw, Phys. Rev. Lett. **96**, 106601 (2006).

[19] V. Gulbinas, R. Kananavičius, L. Valkunas, and H. Bässler, Phys. Rev. B **66**, 233203 (2002).

[20] J. Cabanillas-Gonzalez, T. Virgili, A. Gambetta, L. Lüer, G. Lanzani, T. D. Anthopoulos, and D. M. de Leeuw, Phys. Rev. B **75**, 045207 (2007).

[21] R. Hausermann, E. Knapp, M. Moos, N. Reinke, T. Flatz, and B. Ruhstaller, J. Appl. Phys. **106**, 104507 (2009).

[22] R. C. I. MacKenzie, T. Kirchartz, G. F. A. Dibb, and J. Nelson, J. Phys. Chem. C **115**, 9806 (2011).

[23] H. Bassler, Phys. Status Solidi B **175**, 15 (1993).

[24] B. Bohnenbuck, E. von Hauff, J. Parisi, C. Deibel, and V. Dyakonov, J. Appl. Phys. **99**, 024506 (2006).

[25] Y. Roichman and N. Tessler, Appl. Phys. Lett. **80**, 1948 (2002).

[26] F. F. Stelzl and U. Würfel, Phys. Rev. B **86**, 075315 (2012).

[27] N. Tessler and Y. Roichman, Org. Electron. **6**, 200 (2005).

[28] T. Kirchartz, B. E. Pieters, J. Kirkpatrick, U. Rau, and J. Nelson, Phys. Rev. B **83**, 115209 (2011).

[29] A. Foertig, J. Rauh, V. Dyakonov, and C. Deibel, Phys. Rev. B **86**, 115302 (2012).

[30] J. Nelson, Phys. Rev. B **67**, 155209 (2003).

[31] P. Peumans, A. Yakimov, and S. R. Forrest, J. Appl. Phys. **93**, 3693 (2003).

[32] G. F. Burkhard, E. T. Hoke, and M. D. McGehee, Adv. Mater. **22**, 3293 (2010).

[33] P. B. Johnson and R. W. Christy, Phys. Rev. B **6**, 4370 (1972).

[34] J. Cabanillas-Gonzalez, G. Grancini, and G. Lanzani, Adv. Mater. **23**, 5468 (2011).

[35] G. Cerullo, S. Stagira, M. Nisoli, S. De Silvestri, G. Lanzani, G. Kranzelbinder, W. Graupner, and G. Leising, Phys. Rev. B **57**, 12806 (1998).

[36] A. Devizis, K. Meerholz, D. Hertel, and V. Gulbinas, Phys. Rev. B **82**, 155204 (2010).

[37] A. Devižis, A. Serbenta, K. Meerholz, D. Hertel, and V. Gulbinas, Phys. Rev. Lett. **103**, 027404 (2009).
[38] A. Devižis, K. Meerholz, D. Hertel, and V. Gulbinas, Chem. Phys. Lett. **498**, 302 (2010).
[39] W. Graupner, G. Cerullo, G. Lanzani, M. Nisoli, E. J. W. List, G. Leising, and S. De Silvestri, Phys. Rev. Lett. **81**, 3259 (1998).
[40] F. Etzold, I. A. Howard, R. Mauer, M. Meister, T.-D. Kim, K.-S. Lee, N. S. Baek, and F. Laquai, J. Am. Chem. Soc. **133**, 9469 (2011).
[41] L. M. Andersson, A. Melianas, Y. Infahasaeng, Z. Tang, A. Yartsev, O. Ingans, and V. Sundström, J. Phys. Chem. Lett. **4**, 2069 (2013).
[42] F. Etzold, I. A. Howard, N. Forler, D. M. Cho, M. Meister, H. Mangold, J. Shu, M. R. Hansen, K. Mllen, and F. Laquai, J. Am. Chem. Soc. **134**, 10569 (2012).
[43] See Supplemental Material at http://link.aps.org/supplemental/10.1103/PhysRevB.89.195307 for a more detailed description of the model.